







Temperature-dependent spin polarization of Heusler Co_2MnSi from the disordered local-moment approach: Effects of atomic disordering and nonstoichiometry

Kenji Nawa ^{1,*} Ivan Kurniawan ^{1,2} Keisuke Masuda ¹ Yoshio Miura ^{1,3}
Christopher E. Patrick ^{4,5} and Julie B. Staunton ⁴

¹Research Center for Magnetic and Spintronic Materials, National Institute for Materials Science (NIMS),
1-2-1 Sengen, Tsukuba 305-0047, Japan

²Graduate School of Science and Technology, University of Tsukuba, 1-1-1 Tennodai, Tsukuba, 305-8577, Japan

³Center for Spintronics Research Network (CSRN), Graduate School of Engineering Science, Osaka University, 1-3 Machikaneyama,
Toyonaka, Osaka 560-8531, Japan

⁴Department of Physics, University of Warwick, Coventry CV4 7AL, United Kingdom

⁵Department of Materials, University of Oxford, Oxford OX1 3PH, United Kingdom



(Received 30 April 2020; accepted 24 July 2020; published 18 August 2020)

Half-metallic ferromagnets have been widely investigated by first-principles density-functional theory (DFT) calculations, but extending such studies to investigate spin-polarization at finite temperatures is still challenging due to the difficulty of incorporating temperature effects appropriately. We present DFT calculations, based on a Green's function formulation, which include thermal effects via the disordered local-moment method to address this issue. The calculations are carried out for Heusler Co_2MnSi alloys in order to investigate the temperature dependence of spin polarization, where atomic-disordering and nonstoichiometric effects are taken into account. Our results show that the spin polarization strongly depends on temperature and that a Co d -orbital effect plays a key role in this effect. Furthermore, we find that the temperature-dependent spin polarization of Co_2MnSi can be improved by reducing the Co content and incorporating extra Mn.

DOI: [10.1103/PhysRevB.102.054424](https://doi.org/10.1103/PhysRevB.102.054424)

I. INTRODUCTION

Magnetoresistive devices that show a different resistance depending on the relative magnetization direction of two ferromagnetic electrodes can be applied to nonvolatile magnetic random access memories [1,2] and highly sensitive magnetic sensors [3]. Half-metallic ferromagnets (HMFs) having 100% spin polarization (P) at the Fermi level [4–7] are key materials as sources of highly spin-polarized current in magnetoresistive devices. Among the HMFs, Co-based Heusler alloys Co_2YZ —where Y is a transition metal and Z is a main-group element—are promising due to their high Curie temperatures above room temperature (RT) [7] and robustness of high P against atomic disordering [8,9]. Many experiments on magnetoresistive effects have been performed for magnetic devices containing Co_2YZ [10–23]. For current-perpendicular-to-plane giant magnetoresistive (CPP-GMR) devices, large magnetoresistance (MR) ratios over 57% at RT and 183% at 10 K have been observed using epitaxial $\text{Co}_2\text{Fe}(\text{Ga}_{0.5}, \text{Ge}_{0.5})$ (CFGG) layers [15]. These MR ratios were enhanced to 82% at RT and to 285% at 10 K by inserting a NiAl layer into the CFGG/Ag interface [16]. For magnetic tunneling junctions (MTJs), Yamamoto and coworkers have made systematic

studies of the tunneling magnetoresistance (TMR) ratio and demonstrated high values of 2010% at 4.2 K and 335% at RT in a Co_2MnSi (CMS)/MgO/CMS MTJ with Mn-rich composition for the electrodes [23] and values of 2610% at 4.2 K and 429% at RT in a $\text{Co}_2(\text{Mn,Fe})\text{Si}/\text{MgO}/\text{Co}_2(\text{Mn,Fe})\text{Si}$ MTJ [24].

While large TMR ratios have been observed in MTJ with half-metallic Co_2YZ , these TMR ratios significantly decrease with increasing temperature (T). One possible factor for the reduction of TMR ratio is the T dependence of bulk electronic states of Co_2YZ around the Fermi level in the minority-spin half-metallic gap. Chioncel *et al.* discussed the T dependence of the density of states (DOS) of bulk CMS on the basis of density-functional theory (DFT) combined with dynamical mean-field theory (DMFT) to provide a local self-energy to describe nonquasiparticle states [25]. They found that the T dependence of the total DOS in the bulk region can be attributed to the appearance of nonquasiparticle states around the half-metallic gap at finite temperatures. The total DOS they calculated depended on T , leading to a significant reduction of the spin polarization P with increasing temperature. On the other hand, valence-band electronic structures of bulk CMS have been investigated by hard x-ray photoelectron spectroscopy (HAXPES) by Miyamoto *et al.* [26]. In that experiment, the valence band photoemission spectra at 30 K were in good agreement with the DFT band structure calculation results at zero temperature. Furthermore, no distinct T dependence has been observed for the valence band spectra, which, in DMFT calculations, appears in the total DOS below the Fermi level. These results indicate that the T dependence

*nawa.kenji@nims.go.jp

of the DOS of bulk CMS is rather small and cannot explain the reduction of the TMR ratio at RT.

The other possible cause for the low TMR ratio at RT is an effect of spin-flip scattering through the interface states promoted by magnetic excitations at finite temperature. Mavropoulos *et al.* argued that if there are the interface states in a MTJ, they can contribute to the conductance for antiparallel magnetization because of the spin-flip scattering [27]. In fact, in our previous work, we have showed that the CMS/MgO interface is not half-metallic and has interface states in the half-metallic gap of the minority-spin states originating from the nonbonding $3d$ orbitals of interfacial atoms [28]. Furthermore, Sakuma *et al.* showed from first-principles calculations that the exchange coupling of interfacial Co spins at the CMS/MgO(001) interface is relatively small compared to that of bulk CMS [29], leading to fluctuation of the interfacial Co spin moments at finite temperatures. The effect of spin fluctuations on TMR was investigated in our previous work, where the spin-flip scattering by interface noncollinear magnetic structures due to fluctuations of the Co spin moments significantly reduces the TMR ratios of CMS-based MTJs with MgO barrier [30].

Hu *et al.* investigated the T dependence of tunneling conductance with parallel and antiparallel magnetizations, $G_P(T)$ and $G_{AP}(T)$, of MTJs with CMS/MgO/CMS to elucidate the origin of the T dependence of TMR [31]. They found that $G_P(T)$ shows a characteristic feature, where it first decreases with increasing T before growing larger with further increase of T , while $G_{AP}(T)$ simply increases as T is increased. To understand the characteristic T dependence of $G_P(T)$, they developed a model that took into account both spin-conserving elastic tunneling by Shang [32] and spin-flip inelastic tunneling via magnons by extending the original Zhang model [33]. The Zhang model accounts for the T dependencies of $G_P(T)$ and $G_{AP}(T)$ by including spin-flip inelastic tunneling via thermally excited magnons and an assumed T -independent spin polarization of ferromagnetic electrodes, while the Shang model accounts for the spin-conserving elastic tunneling and reduction of the spin polarization of ferromagnetic electrodes with increasing T . However, at the present stage, the T dependence of the spin-polarization of bulk Co_2YZ is still unknown from the viewpoint of first principles modeling. Therefore in order to understand the origin of the T dependence of $G_P(T)$, $G_{AP}(T)$, and TMR ratio, it is important to elucidate the electronic structure of bulk Co_2YZ at finite temperature.

Calculation of electronic structures based on DMFT [25] is one of the powerful methods to investigate the magnetism at finite temperature. However, because Co_2YZ exhibits itinerant electron magnetism, the strongly correlated electronic picture of DMFT may not be necessarily required to describe magnetic properties. The combination of DFT and classical statistical physics of “local moments” can often give an appropriate description of the finite temperature behavior of itinerant electron systems. The disordered local-moment (DLM) method which treats spin fluctuations modelled as local moments within a mean-field approximation, has been developed [34–43] and successfully applied to describe finite-temperature magnetic anisotropy in $L1_0$ -FePt [35,36] and in rare-earth- Co_5 permanent magnets [37–39] and the magnetocaloric properties of FeRh alloys [40,41].

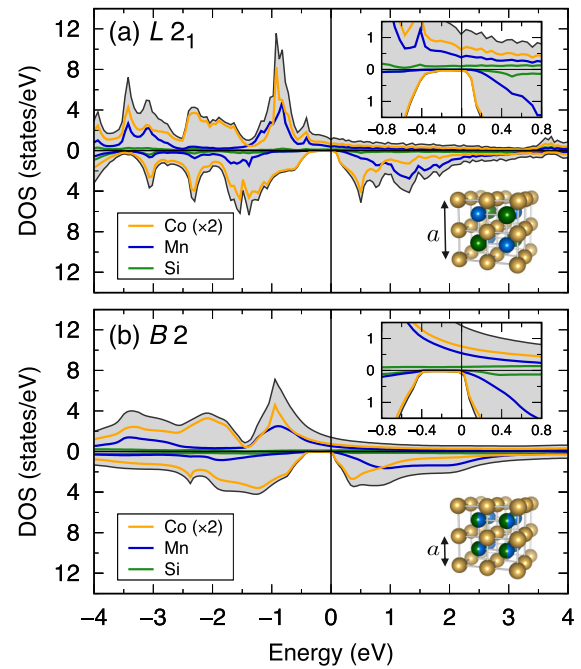


FIG. 1. The DOS for CMS in (a) $L2_1$ and (b) $B2$ structures at $T = 0$ K. The total DOS is shown as filled area and the local DOS is projected on Co (yellow), Mn (blue), and Si (green), respectively. The upper and lower areas show the majority- and minority-spin states and the top-right insets focus on around the Fermi level. The local DOS of Co is multiplied by 2 because two Co atoms exist in the unit cell. The $L2_1$ and $B2$ crystal structures are illustrated in the bottom right of (a) and (b), respectively, where yellow, blue, green, and blue-green bicolor circles indicate Co, Mn, Si, and intermixed-Mn/Si atoms, respectively.

The DLM method is a proven approach for calculating T -dependent spin-polarized electronic structures in magnetic materials whose dominant thermally induced spin fluctuations can be modelled in terms of significant local spin moments. In Co_2YZ a large local-spin moment establishes on the Y sites and so the DLM can be used to describe the T dependence of its spin polarization. To date, DLM-based studies have been applied to possible HMFs. A half-Heusler NiMnSb was the subject of the first attempt which was carried out by Ležaić *et al.* in 2006 [44]. A cubic MnSb phase was later investigated and it was clarified that its spin polarization reduction at RT is much smaller than that of NiMnSb. The cubic-phase crystal growth, of namely c -MnSb, was demonstrated by molecular beam epitaxy [45].

In the present work, we focus on the full Heusler CMS alloy, which is one of the putative HMF materials which is closest to industrial applications, to investigate the spin polarization at finite temperature via first-principles DFT calculations combined with the DLM method, where effects of atomic disordering and nonstoichiometry are taken into account. Our calculations demonstrate that the spin polarization strongly depends on the temperature, where the Co d orbital associated with the nominal X site in the $X_2\text{YZ}$ formula plays a key role. This suggests that the temperature dependence will be varied by changing the Co content in CMS. Thus, we investigate the temperature dependence of

TABLE I. The number of valence electrons, N_{val} , the employed lattice constant a (Å), and results of spin magnetic moments m_{spin} (μ_B) and spin polarization P (%) at $T = 0$ K for the $L2_1$ and $B2$ structures. The a for the $L2_1$ system is taken from Ref. [46] and that for $B2$ is half of this. P is evaluated from Eq. (1).

	N_{val}	a (Å)	m_{spin} (μ_B)				P (%)
			Co	Mn	Si	Total	
$L2_1$	29.000	5.645	1.016	3.042	-0.073	5.000	91.6
$B2$	14.500	2.822	1.007	3.059	-0.074	2.499	84.9

spin polarization of Mn-rich and Mn-poor CMS alloys. In addition, we illustrate how the T -dependent spin polarization can be described well by Bloch's $T^{3/2}$ law, $P \propto (1 - T^{3/2})$, especially for the itinerant electrons that contribute to the tunneling conductance in the MTJ devices.

II. MODEL AND METHOD

A model of the $L2_1$ Heusler structure, which has four atoms arranged on interpenetrating fcc sublattices, i.e., (in units of the lattice constant) a basis of two Co atoms at $(1/4, 1/4, 1/4)$ and $(3/4, 3/4, 3/4)$, one Mn atom at $(0, 0, 0)$ and one Si atom at $(1/2, 1/2, 1/2)$ as illustrated in inset of Fig. 1(a). The lattice constant is assumed to be the experimental value [46], as listed in Table I. In the $B2$ structure the Mn and Si atoms are intermixed randomly at Y and Z sites in Co_2YZ , hence the lattice can be given by the CsCl crystal structure with the lattice constant at half of the $L2_1$ structure [see inset in Fig. 1(b)]. The details for nonstoichiometric structures which are identified by the site-specific formula unit (SSFU) composition model [47,48] are given in Sec. III C. All models treated in present work are assumed to have cubic structures and lattice distortion is excluded.

The computational procedures in our work are divided into two steps. First, the spin-polarized ground-state electronic structures, where the local magnetic moments are ferromagnetically ordered in a collinear configuration, are obtained ($T = 0$ K). The DFT calculations are performed by means of the multiple-scattering Green's function formalism of the Korringa-Kohn-Rostoker (KKR) method [49,50] as implemented in the HUTSEPOT code [51] using the local-spin density approximation (LSDA) of Perdew and Wang [52] for the exchange-correlation term. The atomic-sphere approximation (ASA) is used to determine the Kohn-Sham potential with the equilibrium ASA radius of $2.31 a_B$ for all atoms. Both the core and valence electrons are treated within the scalar-relativistic approximation and the maximum value of the orbital angular momentum $\ell_{\text{max}} = 3$ is used to expand the scattering matrices in a basis of spherical harmonics.

Second, the effects of finite temperature are introduced using the DLM method [34]. The finite temperature effects are captured in terms of fluctuations of local moments, which are assigned to each transition metal site in the given unit cell and whose timescale of stabilization is slower than the electron motion [34]. Using the ground-state potential generated in the first step as the "frozen" potential, the fully relativistic Kohn-Sham-Dirac equation is solved non-self-consistently within the ASA. We give a brief review of the DLM approach in the

Appendix since details including technical aspects have been given in previous works [34–43].

Atomic disorder is described by the coherent potential approximation (CPA) [53–55]. Numerical Brillouin zone (BZ) integrations are performed by using special k -point meshes of $20 \times 20 \times 20$ for self-consistent field calculations and $50 \times 50 \times 50$ for DOS calculations. Note that the latter k -point mesh is found to be sufficient to suppress numerical fluctuation in evaluating the spin polarization P given by

$$P = \frac{D^\uparrow(E_F) - D^\downarrow(E_F)}{D^\uparrow(E_F) + D^\downarrow(E_F)} \times 100 (\%), \quad (1)$$

where $D^\sigma(E_F)$ indicates the DOS at the Fermi energy for spin channel σ ($\sigma = \uparrow$ or \downarrow).

In the discussions below of finite temperature spin-polarized electronic structure we show figures of the site-resolved (local) DOS. The positive (negative) values in the figures show + (−) the average of the DOS spin-polarized parallel (antiparallel) to an overall magnetization direction. In the paramagnetic states ($\mathbf{m}_i = \mathbf{0}$) the majority and minority spin DOS are identical reflecting the zero overall spin polarization of their electronic structures. In the ferromagnetically

TABLE II. The comparison of the Curie temperature, T_C (in units of K), between theories and experiment for $L2_1$ and $B2$ Co_2MnSi . In the literature values, the experimental lattice constant is used except for Refs. [63–65], where the equilibrium value is determined from the calculations.

	Method ^a	T_C (K)
$L2_1$	DLM	1103
	MFA	857 ^b , 1011 ^c , 1162 ^d , 1170 ^e
	RPA	740 ^b , 990 ^f
	MC	780 ^g , 837 ^g , 916 ^h , 980 ⁱ
	Experiment	985 ^j
$B2$	DLM	898

^aMFA: mean-field approximation; RPA: random-phase approximation; MC: Monte Carlo method.

^bReference [60].

^cReference [61].

^dReference [57].

^eReference [65].

^fReference [62].

^gReference [63].

^hReference [64].

ⁱReference [58].

^jReference [59].

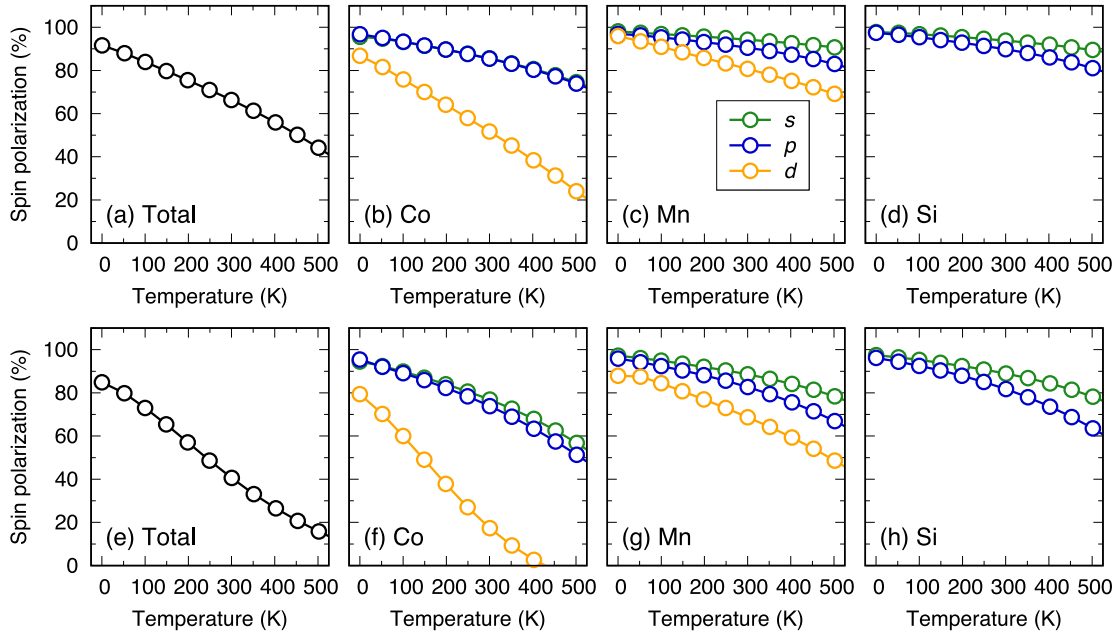


FIG. 2. The T -dependent P for $L2_1$ -type CMS: (a) Total P evaluated from all orbitals, and atom-resolved P is further decomposed into s (green), p (blue), and d (yellow) orbitals for (b) Co, (c) Mn, and (d) Si, respectively. [(e)–(h)] The same for $B2$ -type CMS.

ordered states ($\mathbf{m}_i \neq \mathbf{0}$) the local moments have orientational bias towards the overall magnetization direction which produces internal magnetic fields, i.e., finite Weiss fields. This bias varies as a function of temperature. As a consequence the electronic structures show a temperature-dependent spin-polarization. From values from these densities of states at the Fermi energy, $D^\sigma(E_F)$, which are found by averaging over the local moment orientations with weightings set by the Weiss fields determined by the scheme detailed in the Appendix for a range of temperatures, we are able to describe the temperature dependent spin polarization P from Eq. (1).

III. RESULTS AND DISCUSSION

A. Perfectly ordered $L2_1$ structure

We start with results for the ideal bulk CMS alloy with the perfectly ordered $L2_1$ structure. At $T = 0$ K, our calculations give spin magnetic moments (m_{spin}) of 1.016, 3.042, and $-0.073 \mu_B$ for Co, Mn, and Si, respectively, and total m_{spin} of $5.000 \mu_B$, as listed in Table I. These data are in good agreement with previous LSDA and generalized gradient approximation (GGA) calculations [6,9]. The P evaluated from Eq. (1) is 91.6%, which indicates an almost half-metallic state. Figure 1(a) presents total and local DOS for the $L2_1$ CMS. The total DOS shows the Fermi energy to be located at the edge of the minority-spin conduction bands [see inset in Fig. 1(a)], which as discussed below leads to a value of P less than 100%. Importantly, the minority-spin valence top and conduction bottom bands are governed by the Co d orbitals as previous DFT studies have reported [6,56]. The Si shows very tiny DOS around the Fermi level.

From the integer total m_{spin} , one might expect that we should observe a complete spin polarization of $P = 100\%$, rather than 91.6%. We have confirmed that this discrepancy is not due to the truncation of the angular momentum basis [6

but rather derives from the numerical details of computing the DOS. Here we obtain the DOS from the Green's function calculated at energies including a small, finite imaginary part; a small (large) value of this imaginary part affects the DOS with sharp (broad) peaks. In the present calculations, $\text{Im}(E)$ of 5×10^{-4} Ry was employed and this left a tail of the conduction-bottom bands at the Fermi level. We confirmed that using a smaller value of $\text{Im}(E)$, $\sim 10^{-5}$ Ry, increases the P to almost 100% due to the DOS showing significantly sharper features. However, the computational effort in performing such calculations increases dramatically due to the very dense k -point mesh required to obtain a well-described DOS. Since our primary focus is on the T -dependent behavior of spin polarization in this study, we here discuss the results obtained from $\text{Im}(E) = 5 \times 10^{-4}$ Ry in the DOS calculation.

The Curie temperature, T_C , is determined within the DLM framework [38]. The potential energy $\langle \Omega_0 \rangle_T$ in Eq. (A9) is expanded in terms of the order parameters of local moment at each transition metal sublattices. Around the T_C ($m_i \rightarrow 0$), the potential is truncated at second order as

$$\langle \Omega_0 \rangle_T \approx -\frac{1}{2} J_{\text{Co-Co}} m_{\text{Co}}^2 - J_{\text{Co-Mn}} m_{\text{Co}} m_{\text{Mn}} - \frac{1}{2} J_{\text{Mn-Mn}} m_{\text{Mn}}^2. \quad (2)$$

Performing derivatives of $\langle \Omega_0 \rangle_T$ with respect to the order parameter m_i [Eq. (A9)], we get the Weiss field in matrix form

$$\begin{pmatrix} h_{\text{Co}} \\ h_{\text{Mn}} \end{pmatrix} = \begin{pmatrix} \frac{1}{2} J_{\text{Co-Co}} & \frac{1}{2} J_{\text{Co-Mn}} \\ J_{\text{Co-Mn}} & J_{\text{Mn-Mn}} \end{pmatrix} \begin{pmatrix} m_{\text{Co}} \\ m_{\text{Mn}} \end{pmatrix}, \quad (3)$$

where the denominator of two accounts for the multiplicity of two equivalent Co atoms. The exchange constant J_{ij} parameters can be obtained by fitting the $\{h_i\}$ values calculated from a training set of $\{m_i\}$ using a least-squares method. Equation (3) is then solved as an eigenvalue problem by assuming $m_i \rightarrow 0$ limit; i.e., $m_i = L(\lambda_i) = L(\beta h_i) \rightarrow \beta h_i/3$, and the T_C is

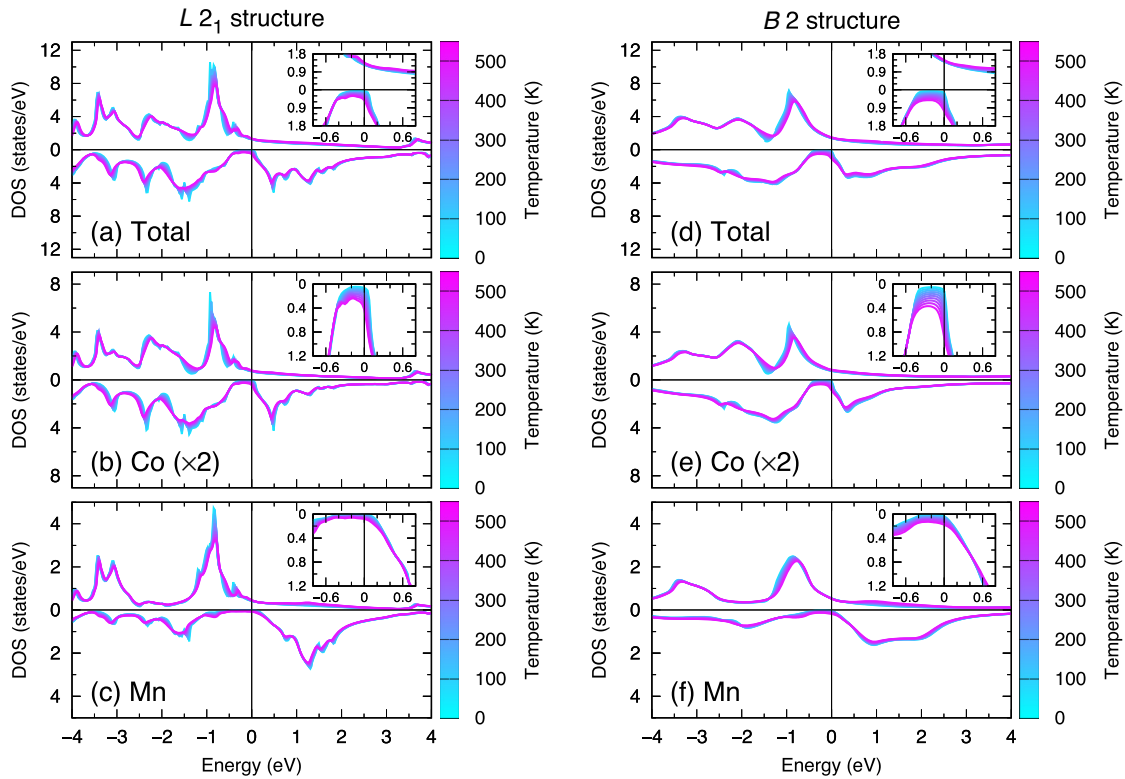


FIG. 3. The T -dependent DOS for $L2_1$ -type CMS: (a) Total DOS and local DOS of (b) Co and (c) Mn. [(d)–(f)] The same for $B2$ -type CMS. The upper and lower areas in each panel are the majority- and minority-spin states, and the insets focus on the Fermi level; both majority and minority states for total DOS and only minority states for local DOS of Co and Mn.

estimated from the smallest β value. In principle T_C might also be calculated from iteration procedures as done for $T \ll T_C$.

The calculated exchange constants of $J_{\text{Co-Co}}$, $J_{\text{Co-Mn}}$, and $J_{\text{Mn-Mn}}$ are found to be 9.57, 25.40, and 1.03 mRy, respectively. These calculations exhibit a trend in good agreement with the J values obtained using Liechtenstein's approach, Ref. [57]. The T_C of 1103 K for $L2_1$ CMS, evaluated by the DLM calculations, is an overestimate on comparison with experiment ($T_C = 985$ K). Different theoretical approaches have reported T_C for $L2_1$ CMS as compared in Table II; mean-field

approximation (MFA) [60,61], random-phase approximation (RPA) [60,62], and Monte Carlo (MC) simulation [63,64]. Among the MFA studies, reported results vary from 857 to 1162 K [57,60,61,65]. This may be caused by differences in computing exchange interactions, whose summation is required to calculate the T_C , and/or in the DFT implementation. For example, in Ref. [60] the interatomic exchange interactions were calculated by the frozen-magnon approach with noncollinear spin-spiral alignment of the system [66,67]. On the other hand, in Ref. [61] these were evaluated from the ground-state electronic structure calculation by a real-space approach in which the energy change of rotation of magnetization is obtained from the magnetic-force theorem [68,69]. The exchange correlation functional can also affect T_C , the former calculation employed the GGA functional on the basis of augmented spherical wave method with ASA potential but the latter used the LSDA+U method in the full-potential KKR scheme. The GGA and GGA+U methods were used in Refs. [65] and [57], respectively. Despite the differences in the T_C of MFA results, we can see that the T_C obtained from our DLM method shows the same magnitude and agrees well in particular with Ref. [61] ($T_C = 1011$ K), which is also implemented in an all-electron KKR method. Similarly to the above, discrepancies in reported T_C values can also be seen in the RPA and MC results because of the differences of the computational methods.

We plot T dependence of P in Figs. 2(a)–2(d). In Fig. 2(a) the total P reduces as T increases and it becomes $P = 66.3\%$ at $T = 300$ K. Remarkably, a huge reduction in the P is found

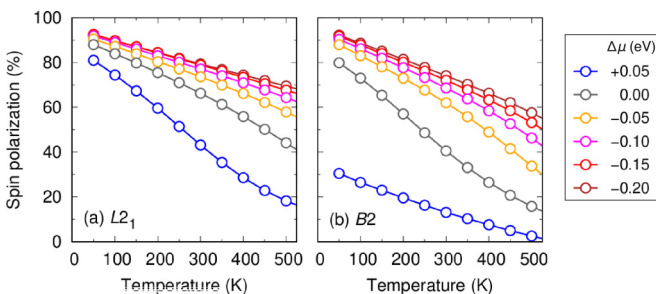


FIG. 4. The T dependence of total P for different chemical-potential shifts $\Delta\mu$ for (a) $L2_1$ and (b) $B2$ Co_2MnSi . The shifts of chemical potential $\Delta\mu$ are given in eV: -0.20 (dark red), -0.15 (red), -0.10 (magenta), -0.05 eV (yellow), and $+0.05$ eV (blue), respectively, where negative (positive) $\Delta\mu$ from the Fermi energy corresponds to hole (electron) doping ($\Delta\mu = 0.00$ eV; gray) in the rigid band model.

TABLE III. The N_{val} (electrons), a (Å), m_{spin} (μ_B), and P (%) at $T = 0$ K for Mn-rich $\text{Co}_2\text{Mn}_\alpha\text{Si}_\beta$ defined by the SSFU expression ($\beta = 1.0$) with its corresponding general expression. Notations of Mn_{Co} and Mn_{Si} indicate the Mn antisite atoms, where excess Mn atoms replace some Co and Si atoms at nominal X and Y site of X_2YZ . The a is taken from Ref. [48].

SSFU	General expression	N_{val}	a (Å)	m_{spin} (μ_B)						P (%)
				Co	Mn_{Co}	Mn	Si	Mn_{Si}	Total	
$\text{Co}_2\text{Mn}_{1.15}\text{Si}_{1.0}$	$(\text{Co}_{1.93}\text{Mn}_{0.07})\text{Mn}(\text{Si}_{0.96}\text{Mn}_{0.04})$	28.976	5.670	1.009	-0.652	3.026	-0.074	3.020	4.975	94.3
$\text{Co}_2\text{Mn}_{1.29}\text{Si}_{1.0}$	$(\text{Co}_{1.86}\text{Mn}_{0.14})\text{Mn}(\text{Si}_{0.93}\text{Mn}_{0.07})$	28.938	5.672	1.013	-0.687	2.999	-0.071	2.989	4.936	94.8
$\text{Co}_2\text{Mn}_{1.44}\text{Si}_{1.0}$	$(\text{Co}_{1.80}\text{Mn}_{0.20})\text{Mn}(\text{Si}_{0.90}\text{Mn}_{0.10})$	28.904	5.676	1.020	-0.715	2.972	-0.069	2.960	4.902	94.7

only for the Co d states. The Co d - P decreases from 86.8% at 0 K to 51.7% at 300 K [Fig. 2(b)], whereas only a small reduction is confirmed in the spin polarization associated with other orbitals including Mn d (over $\sim 70\%$ even at RT) [Figs. 2(c) and 2(d)]. Figures 3(a)–3(c) show the changes of the total and local DOS plots with elevating T . In Fig. 3(a), the profile of the total DOS becomes smoother when T increases, and only the minority-spin states are sensitive to the temperature around the Fermi level, although the majority-spin DOS is hardly changed. This fact lets us focus only on the minority-spin states for the discussion hereafter. A remarkable increase in the minority DOS at the Fermi level appears only in the Co local DOS [Fig. 3(b)] since the band gap between the valence and conduction states in Co is narrower than in Mn. The results for Si are not presented in Fig. 3 since the Si DOS is not dominant as mentioned above. One may expect the changes of the DOS to be relatively modest, as observed here, since the investigated temperatures are much lower than T_C . Further increasing the temperature leads to an increasingly smooth DOS profile, approaching a non-spin-polarized electronic structure at T_C .

Experimentally, the spin polarization can be estimated by the Jullière model where the TMR is determined by the “bulk” spin polarization of the total DOS of the ferromagnetic electrodes at the Fermi level [70]. A spin polarization of 89% is observed at 2 K but it drastically reduces by almost half at RT [17,71]. The experimentally observed reduction in spin polarization from low temperature to RT is quite significant compared to that found by our calculations. This difference likely derives from the magnetic impurities present at the Heusler/insulator interface which cause spin-flip inelastic tunneling [32,72], which are missing from our calculations.

Our T -dependent total DOS [Fig. 3(a)] shows a high peak in the majority-spin states at around 0.9 eV below the Fermi level and, very importantly, the peak-shift width is quite narrow in energy by ≈ 0.1 eV even when the temperature is raised to 500 K. This result is reasonably consistent with the HAXPES observation [26], where the valence band structures at $T = 30$ and 300 K are almost identical, which was not observed in the DFT+DMFT calculation results. [25]

TABLE IV. The same as Table III but for Mn-poor $\text{Co}_2\text{Mn}_\alpha\text{Si}_\beta$ ($\beta = 1.0$). Notations of Co_{Mn} and Si_{Mn} indicate the Co and Si antisite atoms, where the deficiencies in Mn atoms are made up by Co and Si atoms at Y site, respectively.

SSFU	General expression	N_{val}	a (Å)	m_{spin} (μ_B)						P (%)
				Co	Mn	Co_{Mn}	Si_{Mn}	Si	Total	
$\text{Co}_2\text{Mn}_{0.85}\text{Si}_{1.0}$	$\text{Co}_2(\text{Mn}_{0.88}\text{Co}_{0.08}\text{Si}_{0.04})\text{Si}$	29.039	5.658	1.030	2.978	1.426	-0.065	-0.059	4.740	27.3

Figure 4(a) presents the temperature dependencies of the total P for different chemical potentials $\Delta\mu$ within a rigid band model. For a negative shift of the chemical potential from the Fermi energy, $\Delta\mu < 0$, P becomes higher in value as $\Delta\mu$ decreases. On the other hand, a positive shift, $\Delta\mu > 0$, lowers P significantly. Thus, Fermi-level tuning by hole-doping is advantageous to suppress the P reduction at finite T as found in the stoichiometric $L2_1$ material. We note that, however, even for $\Delta\mu < 0$, enhancement of P might not be realized for a negative shift of over ~ 0.5 eV due to the Fermi-level position touching the minority spin valence bands [results are not shown in Fig. 4(a) for simplicity]. These facts agree with experiment, in which the spin polarization is improved by doping a certain quantity of holes by partial Al substitution with Si in CMS in the combinatorial sputtering technique [73].

B. Disordered $B2$ structure

The total magnetization, m_{spin} , is obtained as $2.499 \mu_B$ for the $B2$ -type CMS at $T = 0$ K, and the results for the atomic-decomposed m_{spin} are summarized in Table I. Since the Mn and Si are intermixed by 50:50 composition in the $B2$ structure with half the lattice constant of $L2_1$, the m_{spin} values are multiplied by their compositions for each Mn and Si, so that the summation of local moments corresponds to the total m_{spin} . The DOS calculated by the CPA-KKR scheme is presented in Fig. 1(b). Clearly, the DOS profile is widely smeared compared to the $L2_1$ alloy, in which crystal momentum $\hbar\mathbf{k}$ is no longer the good quantum number and Bloch spectral function is broadened in energy due to the lifetime effect. Although the half-metallic gap in the minority-spin states is preserved in the $B2$ structure as in $L2_1$, the absolute value of minority-spin DOS at the Fermi energy is larger than the $L2_1$ due to the conduction edges touching the Fermi energy. As a result, a rather small P is estimated, $P = 84.9\%$. However, the fact that only a small reduction in P is induced by $B2$ -type atomic disorder at zero temperature is consistent with a previous study carried out for Co_2CrAl [8]. We emphasize that

the feature shared with the $L2_1$ structure is that Co d states are dominant in the minority-spin gap around Fermi energy.

A rather monotonic decrease in the total P is observed in the $B2$ structure and the value becomes less than 40% above RT, as shown in Fig. 2(e). The spin polarizations for each orbital component show that only the Co d - P rapidly decreases and the value is 17.4% at 300 K, as compared in Figs. 2(f), 2(g) and 2(h) for Co, Mn, and Si, respectively. We plot in Figs. 3(d)–3(f) the T -dependent DOS. Figure 3(e) shows that the minority-spin DOS of Co is drastically increased at the Fermi energy, although the change in minority DOS is less in Mn as shown in Fig. 3(f). Consequently, from the results of $L2_1$ and $B2$ structures, the Co d electrons always play a key role in determining the spin polarization in the system at finite temperature because these minority states are located at the valence top and conduction bottom bands. However, importantly, the P reduction at finite temperature is significant in the $B2$ structure compared to the $L2_1$. For example, the $L2_1$ system shows $P = 44.1\%$ at $T = 500$ K but the $B2$ - P is only 15.8%. This is reflected by the difference of the Fermi level position as discussed for the zero-temperature results. The minority-spin DOS is intrinsically larger and is more sensitive to the temperature in the $B2$ structure than in $L2_1$ at the Fermi energy, while the majority DOS has almost the same magnitude and is not changed much as T increases in both, as shown in insets of Figs. 3(a) and 3(d). Similar to the $L2_1$ system, a negative chemical-potential shift, corresponding to $\Delta\mu < 0$, increases P , while a positive shift, $\Delta\mu > 0$, decreases P [Fig. 4(b)].

For T_C estimation in compositionally disordered $B2$ structures, Eq. (3) is modified as

$$\begin{pmatrix} h_{\text{Co}} \\ h_{\text{Mn}} \end{pmatrix} = \begin{pmatrix} J_{\text{Co-Co}} & c_{\text{Mn}} J_{\text{Co-Mn}} \\ J_{\text{Co-Mn}} & c_{\text{Mn}} J_{\text{Mn-Mn}} \end{pmatrix} \begin{pmatrix} m_{\text{Co}} \\ m_{\text{Mn}} \end{pmatrix}, \quad (4)$$

where c_{Mn} indicates the composition of Mn ($c_{\text{Mn}} = 0.5$). The multiplicity factor does not appear compared to Eq. (3), since the $B2$ is a simple cubic lattice including *one* Co occupied sublattice, whereas $L2_1$ has *two* fcc sublattices occupied by Co. The T_C of 898 K is obtained from the $B2$ structure, as summarized in Table II. We speculate that the large reduction of T_C from that of the $L2_1$ structure originates from the intermixing of Mn with much Si (50%), which indicates that the Si p electrons might induce an instability of spin polarization of Mn d electrons at the same atomic site in the alloy. This inference is based on the comparison of $L2_1$ ($T_C = 1103$ K), where no intermixing is included, and the nonstoichiometric systems ($T_C \sim 1000$ K), where the intermixing is incorporated but the composition ratio is quite small compared to the $B2$ structure (the latter system is discussed in detail in Sec. III C).

C. Nonstoichiometric disordered $L2_1$ structure

The SSFU composition model, namely $\text{Co}_2\text{Mn}_\alpha\text{Si}_\beta$, is proposed in Refs. [47] and [48] in order to describe the nonstoichiometry in the thin film assumed in MTJ devices. In detail, the SSFU model accommodates only antisite structural defects but not vacancy defects, and is based on the formation energy analyses by the DFT [9,74]. The Mn_{Co} and Mn_{Si} antisites, where excess Mn atoms replace some Co and Si atoms at nominal X and Z site of X_2YZ , are energetically

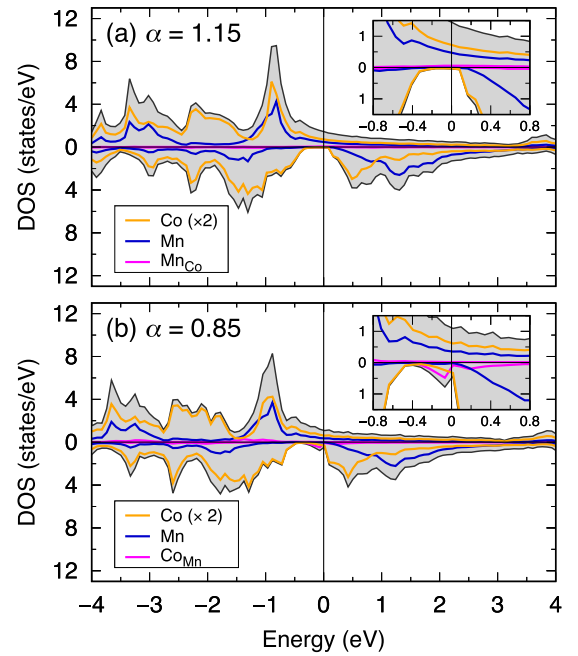


FIG. 5. The same as in Fig. 1 but for (a) Mn-rich $\text{Co}_2\text{Mn}_{1.15}\text{Si}_{1.0}$ and (b) Mn-poor $\text{Co}_2\text{Mn}_{0.85}\text{Si}_{1.0}$ in SSFU.

favorable compared to either vacancy defects at the Co or Si sites. Similarly, Co_{Mn} and Si_{Mn} antisites, where the Y -site Mn is replaced with Co and Si, have lower formation energies than for Mn vacancies. The former results in a Mn-rich thin film system ($\alpha > 1$) and the latter in a Mn-poor ($\alpha < 1$) one. In addition, although theories [9,74] have clarified that Si-deficient nonstoichiometry ($\beta < 1$) can be inferred from energetics, we fixed $\beta = 1.0$ for simplicity throughout the present work. Note that since atomic-vacancy defects are not included in the SSFU model, the site-occupation ratio of 2:1:1 in the given $L2_1$ structure X_2YZ is preserved to be stoichiometric although the atomic ratio of Co:Mn:Si is nonstoichiometric. The nonstoichiometric systems we treat follow the above SSFU model. The SSFU expressions for Mn-rich and Mn-poor $\text{Co}_2\text{Mn}_\alpha\text{Si}_{\beta=1.0}$ are summarized in Tables III and IV, respectively, with the corresponding general expressions. The lattice constants are set to the experimentally measured values in the epitaxially grown thin films of $\text{Co}_2\text{Mn}_\alpha\text{Si}_{1.0}$ on a $\text{MgO}(001)$ substrate [48].

We firstly present the results at $T = 0$ K. For the Mn-rich case, the calculated results are summarized in Table III and confirm that the spins of excess Mn atoms couple with those of Co and Si at respective X and Z sites antiferromagnetically. The m_{spin} of Y -site Mn becomes slightly smaller compared to that in the ideal CMS as the degree of α composition increases. We also find that the evaluated P is greater than the ideal case's value by $\sim 3\%$. This is attributed to the Fermi-level shifting to a lower energy induced by Mn antisites from the stoichiometric $L2_1$ structure. This results in a reduction of the number of occupied valence electrons, N_{val} (see Table III). Figure 5(a) shows the DOS for $\alpha = 1.15$ as an example. The tendency discussed above is consistent with previous calculated results by the all-electron full-potential linearized augmented plane wave method within the GGA [9]. The DOS

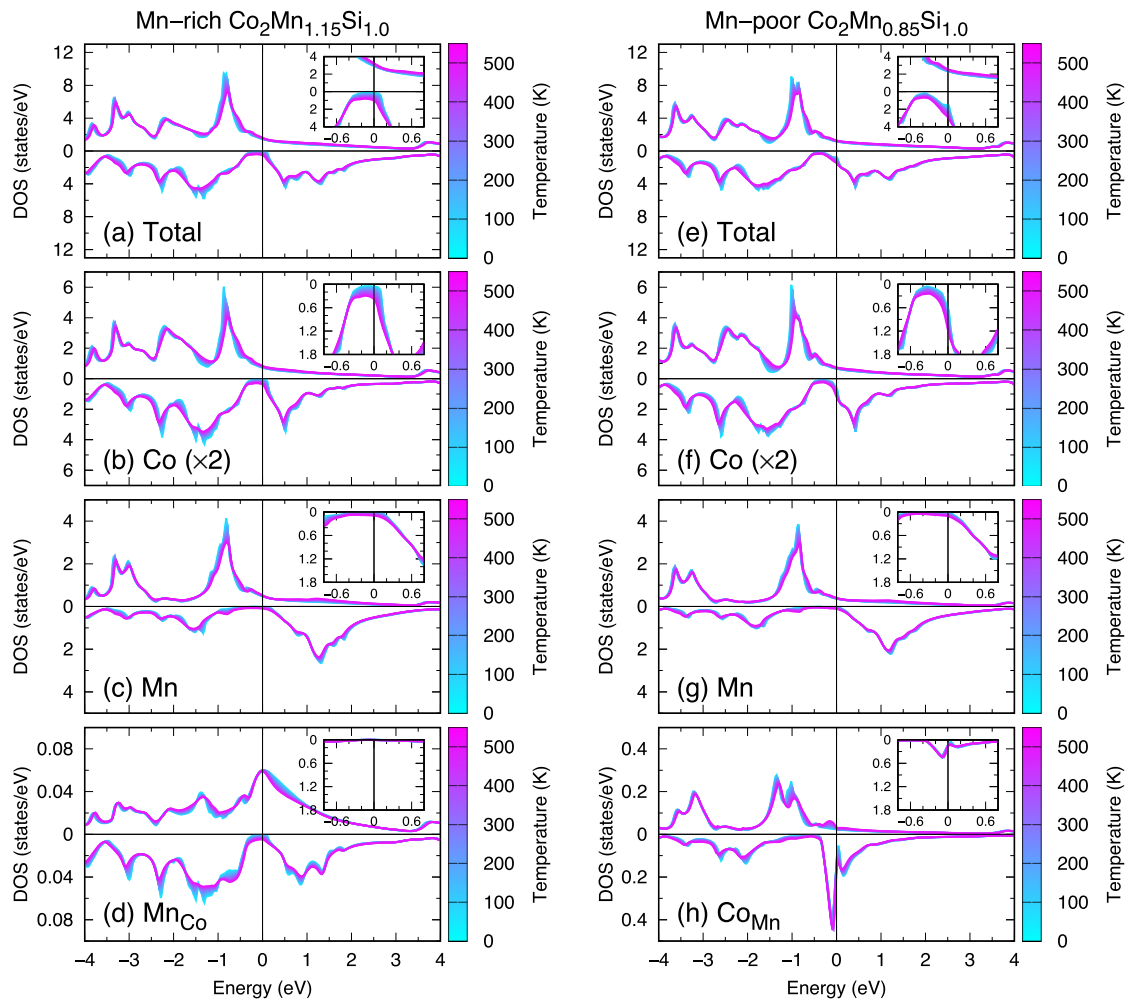


FIG. 6. The same as in Fig. 3 but for [(a)–(d)] Mn-rich $\text{Co}_2\text{Mn}_{1.15}\text{Si}_{1.0}$ and [(e)–(h)] Mn-poor $\text{Co}_2\text{Mn}_{0.85}\text{Si}_{1.0}$. The insets focus on the Fermi level; both majority and minority states for total DOS and only minority spin local DOS of Co, Mn, and antisite Mn_{Co} and Co_{Mn} .

for $\alpha = 1.29$ and 1.44 are not presented in this paper since significant differences from $\alpha = 1.15$ do not appear.

On the other hand, Mn deficiency is detrimental to half-metallicity. We only present the alloy with composition of $\alpha = 0.85$. The Mn m_{spin} on the Y site is reduced compared to that of the stoichiometric $L2_1$ case, and a smaller total m_{spin} is obtained, $4.740 \mu_B$ (see Table IV). The P value is as small as 27.3% at 0 K. From the local DOS plot given in Fig. 5(b), the low P arises from the additional occupied Co d minority-spin states associated with the X site. The Co_{Mn} -antisite defect-induced pseudogap states that appear for the minority states around the Fermi energy also reduce the spin polarization [9]. These lead to $N_{\text{val}} = 29.039$ being greater than the stoichiometric $L2_1$ system (Table IV).

At finite temperature, features similar to those in the stoichiometric $L2_1$ and $B2$ structures are found in Mn-rich $\text{Co}_2\text{Mn}_\alpha\text{Si}_{1.0}$. The minority-spin Co local DOS plays a dominant role in the spin polarization and sensitively increases at the Fermi level, as shown in Fig. 6(b). The change of the Mn-local DOS is smaller than Co's [see Fig. 6(c)]. Additionally, Fig. 6(d) shows that the antisite Mn_{Co} atom does not affect the electronic structure so much around the Fermi energy. The same situation is evident with respect to the Mn_{Si} site

(DOS results are not presented). However, the T dependence of P is indeed improved by adding excess Mn atoms. In Fig. 7(a), the P for Mn-rich CMS is higher than for the perfectly stoichiometric system over the whole temperature range up to 500 K and the reduction of P with increasing temperature becomes less than that for the stoichiometric case owing to the Fermi-level shifting discussed above.

In actual MTJ devices with MgO barriers, it is expected that most of the tunneling of electrons is dominated by the coherent tunneling of itinerant electrons in s and p orbitals [48]. Motivated by this fact, we evaluate the spin polarization using only the sp orbitals, P_{sp} , which we plot in Fig. 7(b). The P_{sp} becomes smaller compared to that of the stoichiometric system as the composition parameter α increases for every temperature up to 500 K. However, we stress that the atomic disorder induced by the Mn-rich composition is superior to $B2$ -type Mn-Si disorder for keeping a high spin polarization of the itinerant sp electrons. We point out that the direct comparison with experimental measurements of spin polarization is difficult even qualitatively. Experimental measurements of the T dependence of TMR in $\text{Co}_\alpha\text{MnSi}_\beta/\text{MgO}/\text{Co}_\alpha\text{MnSi}_\beta$ MTJ, where the Mn composition varies, are available in Refs. [31] and [48]. However, because secondary magnetic

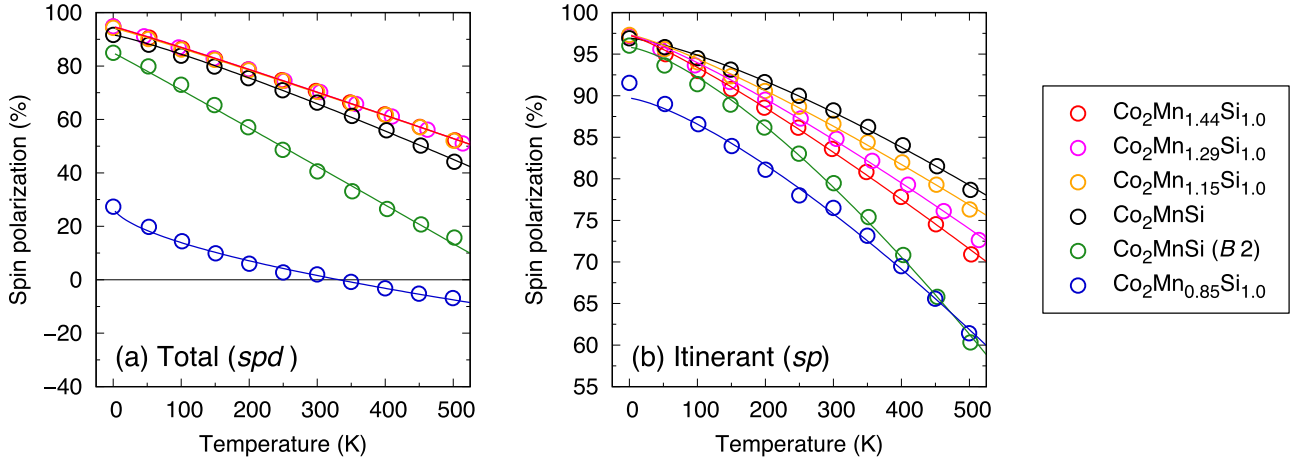


FIG. 7. The T dependencies of (a) total (spd) P and (b) itinerant (sp) P_{sp} for nonstoichiometric Co_2MnSi ; Mn-rich $\text{Co}_2\text{Mn}_\alpha\text{Si}_{1.0}$ with $\alpha = 1.44$ (red), 1.29 (magenta), and 1.15 (yellow), and Mn-poor $\text{Co}_2\text{Mn}_\alpha\text{Si}_{1.0}$ with $\alpha = 0.85$ (blue) in SSFU. Solid lines indicate the fitted curves. The results of stoichiometrically ordered $L2_1$ (black) and disordered $B2$ (green) structures are also plotted for reference.

phases such as nonmagnetic or antiferromagnetic structures may appear when there are excess Mn atoms, the behavior of spin polarization at finite temperature is unclear in terms of the effect of the Mn composition in experiments [48].

Since the X -site Co d electrons and the defect-induced pseudogap states associated with the Co_{Mn} antisite disrupts the half-metallic-like electronic structure, the Mn-poor $\text{Co}_2\text{Mn}_{0.85}\text{Si}_{1.0}$ is incapable of preserving the high spin polarization at finite temperatures. In Figs. 6(e)–6(h), the minority-spin local DOS for Mn and Co_{Mn} do not change much at the

Fermi level when T is increased, on the other hand, the Co d DOS become larger. As a result, P decreases to zero around 300 K and becomes negative afterwards, as shown in Fig. 7(a). The T -dependent P_{sp} is plotted in Fig. 7(b). It can be seen that the Mn-poor alloy also has highly spin-polarized itinerant sp electrons. The comparison of our results with published theoretical values can only be made for $T = 0$ K [48], where we find good agreement.

To get T_C , we solve the eigenvalue problems

$$\begin{pmatrix} h_{\text{Co}} \\ h_{\text{MnCo}} \\ h_{\text{Mn}} \\ h_{\text{MnSi}} \end{pmatrix} = \begin{pmatrix} \frac{1}{2}c_{\text{Co}}J_{\text{Co-Co}} & \frac{1}{2}c_{\text{MnCo}}J_{\text{Co-MnCo}} & \frac{1}{2}J_{\text{Co-Mn}} & \frac{1}{2}c_{\text{MnSi}}J_{\text{Co-MnSi}} \\ \frac{1}{2}c_{\text{Co}}J_{\text{MnCo-Co}} & \frac{1}{2}c_{\text{MnCo}}J_{\text{MnCo-MnCo}} & \frac{1}{2}J_{\text{MnCo-Mn}} & \frac{1}{2}c_{\text{MnSi}}J_{\text{MnCo-MnSi}} \\ c_{\text{Co}}J_{\text{Mn-Co}} & c_{\text{MnCo}}J_{\text{Mn-MnCo}} & J_{\text{Mn-Mn}} & c_{\text{MnSi}}J_{\text{Mn-MnSi}} \\ c_{\text{Co}}J_{\text{MnSi-Co}} & c_{\text{MnCo}}J_{\text{MnSi-MnCo}} & J_{\text{MnSi-Mn}} & c_{\text{MnSi}}J_{\text{MnSi-MnSi}} \end{pmatrix} \begin{pmatrix} m_{\text{Co}} \\ m_{\text{MnCo}} \\ m_{\text{Mn}} \\ m_{\text{MnSi}} \end{pmatrix}, \quad (5)$$

$$\begin{pmatrix} h_{\text{Co}} \\ h_{\text{Mn}} \\ h_{\text{CoMn}} \end{pmatrix} = \begin{pmatrix} \frac{1}{2}J_{\text{Co-Co}} & \frac{1}{2}c_{\text{Mn}}J_{\text{Co-Mn}} & \frac{1}{2}c_{\text{CoMn}}J_{\text{Co-CoMn}} \\ J_{\text{Mn-Co}} & c_{\text{Mn}}J_{\text{Mn-Mn}} & c_{\text{CoMn}}J_{\text{Mn-CoMn}} \\ J_{\text{CoMn-Co}} & c_{\text{Mn}}J_{\text{CoMn-Mn}} & c_{\text{CoMn}}J_{\text{CoMn-CoMn}} \end{pmatrix} \begin{pmatrix} m_{\text{Co}} \\ m_{\text{Mn}} \\ m_{\text{CoMn}} \end{pmatrix}, \quad (6)$$

for Mn-rich and Mn-poor alloys, respectively. The concentrations c_i are given in the second column in Tables III and IV ($i = \text{Co}, \text{MnCo}, \text{and MnSi}$ for the Mn-rich case and $i = \text{Mn}$ and CoMn for the Mn-poor case). The T_C values are summarized in Table V. We find the T_C is slightly lowered from that of the stoichiometric system ($T_C = 1103$ K), and gradually reduces

as the composition α is increased for the Mn-rich case. The Mn-poor system also shows a lower T_C than the stoichiometric one. A similar trend was reported in Co_2FeSi from KKR calculations, in which a reduction in T_C was observed when the Fe composition was varied [75].

Figure 8 presents the calculated exchange-energy constants J_{ij} for nonstoichiometric alloys with the comparison of the stoichiometric $L2_1$ alloy. The atomic compositions of antisites are somewhat smaller than those of nominal sites, thus, we focus on the effective J_{ij} between atoms only at the nominal sites, namely interactions of Co-Co, Co-Mn, and Mn-Mn. The values in Fig. 8 are multiplied according to the atomic compositions. It is clear, for Mn-rich models, that the $J_{\text{Co-Mn}}$ showing the largest value in each model becomes small as the α increases. This trend reflects the decrease of the T_C with increasing α . A similar reduction in $J_{\text{Co-Mn}}$ from the stoichiometric system is also found in Mn-poor $\text{Co}_{0.85}\text{MnSi}_{1.0}$

TABLE V. The calculated T_C for nonstoichiometric $\text{Co}_2\text{Mn}_\alpha\text{Si}_{1.0}$ in the SSFU expression.

	SSFU	T_C (K)
Mn rich	$\text{Co}_2\text{Mn}_{1.15}\text{Si}_{1.0}$	1050
	$\text{Co}_2\text{Mn}_{1.29}\text{Si}_{1.0}$	1023
	$\text{Co}_2\text{Mn}_{1.44}\text{Si}_{1.0}$	1000
Mn poor	$\text{Co}_2\text{Mn}_{0.85}\text{Si}_{1.0}$	1051

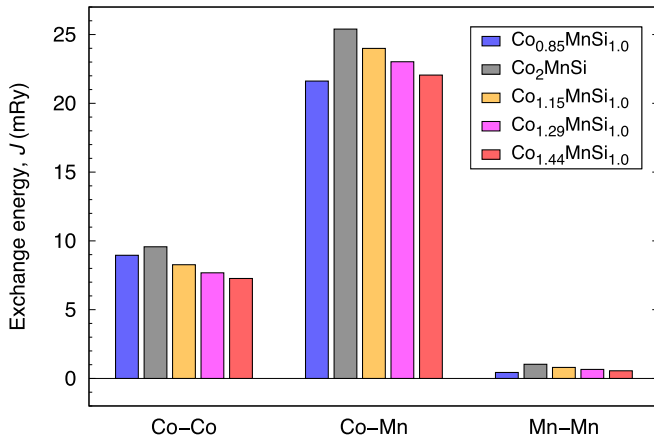


FIG. 8. The calculated J_{ij} of nominal-site Co-Co, Co-Mn, and Mn-Mn interactions for nonstoichiometric alloys; Mn-rich $\text{Co}_2\text{Mn}_\alpha\text{Si}_{1.0}$ with $\alpha = 1.15$ (yellow), 1.29 (magenta), and 1.44 (red), and Mn-poor $\text{Co}_2\text{Mn}_\alpha\text{Si}_{1.0}$ with $\alpha = 0.85$ (blue) in SSFU. The results for stoichiometric $L2_1$ alloy is also presented as a reference (gray).

which also lowers the T_C . Our calculations thus demonstrate that a mixture of the two transition metals on X or Y leads to a decrease in the T_C .

D. Temperature-dependent spin polarization from the DLM method and Bloch's $T^{3/2}$ law

Finally, we mention verifications of the Bloch $T^{3/2}$ law for spin polarization. In the extended Zhang model [31], the T -dependent spin polarization was taken into account using Bloch's law formalism as the Shang model had done [32], i.e., $P(T) = P_0(1 - \eta_M T^{3/2})$, where P_0 is the spin polarization at $T = 0$ K and η_M is a material-dependent interface parameter that determines the spin-polarization reduction with elevating temperature for parallel ($M = P$) and antiparallel ($M = AP$) magnetizations in an MTJ device. This formula has been proposed as an extension from Bloch spin-wave theory that describes magnetization excitation due to low-energy long-range spin waves at the temperatures far below T_C [76]. So far, however, there has been no report for an evidence related to the Bloch-type spin polarization at nonzero temperature from first-principles calculations although the T -dependent behavior of spin polarization is of importance in understanding, especially, tunneling conductance for MTJ in $M = P$. The formalism of the tunneling phenomenon for $M = P$ discussed here corresponds to Eq. (7) in Ref. [31].

The T -dependent spin polarizations are fitted to

$$P(T) = P_0(1 - \eta T^\kappa). \quad (7)$$

TABLE VI. Parameters of η and κ obtained from fitting to Eq. (7) using the spin polarizations of total (spd) and itinerant (sp) orbitals in stoichiometric $L2_1$ and $B2$ structures. η has a unit of Kelvin to the minus κ .

	Total (spd)		Itinerant (sp)	
	η ($\text{K}^{-\kappa}$)	κ	η ($\text{K}^{-\kappa}$)	κ
$L2_1$	3.74478×10^{-4}	1.16069	4.38096×10^{-5}	1.34124
$B2$	1.51584×10^{-3}	1.01670	5.82093×10^{-5}	1.40488

For the η parameter, here, we ignore a difference between the $M = P$ and AP cases, i.e., $\eta = \eta_P = \eta_{AP}$, since the values fitted from the experiments are same in magnitude, typically $\sim 10^{-5}$ [31,77]. The fitting analyses are carried out for both total (spd)- and itinerant (sp)-orbital spin polarizations; the fitting curves are plotted with solid lines in Fig. 7 and the coefficients η and κ are given in Tables VI and VII for stoichiometric and nonstoichiometric systems, respectively. For stoichiometric alloys, from Table VI, our results indicate that the T dependencies of P_{sp} can be characterized well by the Bloch's law rather than those of total P with the parameters $\kappa \sim 3/2$ and $\eta \sim 10^{-5}$. From the total P , the fitted κ values are found to be small especially in the $B2$ alloy, indicating a monotonic P reduction ($\kappa \sim 1$). In the nonstoichiometric alloys, similar to above, the κ parameters from itinerant P_{sp} become closer to $3/2$ than those from total P . The Mn-poor $\text{Co}_2\text{Mn}_{0.85}\text{Si}_{1.0}$ shows quite a small value $\kappa = 0.59422$ from P but this is drastically improved to $\kappa = 1.35739$ for P_{sp} . This is because the reduced total P is attributed mainly to the Co d state around Fermi level, as discussed in earlier sections.

Considering the fact that the major contribution to the electron tunneling is not for the localized d states but for the itinerant sp states and that the T -dependent tunneling conductance of $M = P$ magnetization has been successfully demonstrated by the extended Zhang model which employs the Bloch-based spin polarization even in the Mn-poor alloy [31], precise calculations of the thermal dependence of the itinerant spin polarization is crucial to understand the TMR at finite temperature *ab initio*. However, our DLM method does not adhere to Bloch's $T^{3/2}$ law in terms of the parameter κ , owing to the classical model it uses for the fluctuation of *single-site* local moments, whereas Bloch's law describes the low temperature thermal excitations due to the *many-body* spin waves.

IV. SUMMARY

In summary, first-principles KKR calculations combined with the CPA and DLM methods have been performed to clarify the spin polarization at finite temperature in the Heusler Co_2MnSi , where effects of atomic disorder and nonstoichiometry have been considered. We have found that all the systems show significant reduction of the spin polarization when the temperature is increased. The mechanism was understood to be connected to the behavior of Co d states because these states are located around the minority-spin gap around the Fermi energy. The differences in the decay of the spin polarization with regard to temperature in the stoichiometric $L2_1$ and $B2$ structures are governed by the DOS of minority-spin states near the Fermi energy. We also considered nonsto-

TABLE VII. The same as Table VI but for nonstoichiometric Mn-rich and -poor $\text{Co}_2\text{Mn}_\alpha\text{Si}_{1.0}$ in the SSFU expression.

SSFU		Total (<i>spd</i>)		Itinerant (<i>sp</i>)	
		η ($\text{K}^{-\kappa}$)	κ	η ($\text{K}^{-\kappa}$)	κ
Mn rich	$\text{Co}_2\text{Mn}_{1.15}\text{Si}_{1.0}$	6.48535×10^{-4}	1.04912	1.10423×10^{-4}	1.21517
	$\text{Co}_2\text{Mn}_{1.29}\text{Si}_{1.0}$	6.56393×10^{-4}	1.04806	1.29593×10^{-4}	1.21041
	$\text{Co}_2\text{Mn}_{1.44}\text{Si}_{1.0}$	6.59337×10^{-4}	1.04707	1.71988×10^{-4}	1.18055
Mn poor	$\text{Co}_2\text{Mn}_{0.85}\text{Si}_{1.0}$	3.17618×10^{-2}	0.59422	6.73572×10^{-5}	1.35739

ichiometric $\text{Co}_2\text{Mn}_\alpha\text{Si}_\beta$ in the SSFU model, in which the composition parameter α varies from 0.85 to 1.44 and β was fixed at 1. Our calculations clarified that the alloys with Mn-rich composition possess high spin polarization at finite temperatures owing to the Fermi-level shifting to lower energy compared to that of the stoichiometric $L2_1$ system, whereas the Mn-poor alloy shows low spin polarization owing to the finite DOS at Fermi level that originates from nominal X -site Co and antisite Co_{Mn} states. We found that the temperature dependence of the total P can be improved in Mn-rich CMS because of the reduction in Co content. Moreover, we discussed Bloch's $T^{3/2}$ law from fitting the T dependence of the spin polarization. The decrease of the spin polarization with T increase can be described well by this relation, especially, for the itinerant sp electrons, although there is a small discrepancy between our MFA-based DLM approach and many-body Bloch's law.

ACKNOWLEDGMENTS

Authors are grateful to Hisazumi Akai at the University of Tokyo, Munehisa Matsumoto at High Energy Accelerator Research Organization, and S. Mitani and Y. Sakuraba at NIMS for fruitful discussions and suggestions. Work at NIMS is partly supported by Grants-in-Aid for Scientific Research (S) (Grants No. JP16H06332 and No. JP17H06152) from the Japan Society for the Promotion of Science, and Center for Spintronics Research Network (CSRN), Osaka University. Work at UoW was supported by EPSRC (UK) Grants No. EP/M028941/1 and No. EP/K032852/1. The computations were performed on a Numerical Materials Simulator at NIMS and on the facilities of the Supercomputer Center, the Institute for Solid State Physics, the University of Tokyo.

APPENDIX: DLM CALCULATIONS FOR FINITE TEMPERATURE

We here provide a brief review of the DLM approach, with further details provided in previous works [34–43]. A system, which has N local moments at corresponding magnetic sublattices, is specified as $\{\hat{\boldsymbol{e}}_i\} = \{\hat{\boldsymbol{e}}_1, \hat{\boldsymbol{e}}_2, \dots, \hat{\boldsymbol{e}}_N\}$, where the magnetization direction is given by $\hat{\boldsymbol{e}}_i = (\sin \theta_i \cos \phi_i, \sin \theta_i \sin \phi_i, \cos \theta_i)$ at each site i . For the thermodynamic grand potential $\Omega(\{\hat{\boldsymbol{e}}_i\})$ of the orientations $\{\hat{\boldsymbol{e}}_i\}$, the probability distribution function is given by

$$P(\{\hat{\boldsymbol{e}}_i\}) = \frac{1}{Z} \exp[-\beta \Omega(\{\hat{\boldsymbol{e}}_i\})] \quad (\text{A1})$$

with the partition function

$$Z(\{\hat{\boldsymbol{e}}_i\}) = \int \dots \int \exp[-\beta \Omega(\{\hat{\boldsymbol{e}}_i\})] d\hat{\boldsymbol{e}}_1 \dots d\hat{\boldsymbol{e}}_N. \quad (\text{A2})$$

Here $1/\beta = k_B T$ and k_B is the Boltzmann constant. The grand potential $\Omega(\{\hat{\boldsymbol{e}}_i\})$ could, in principle, be determined by finite-temperature constrained DFT calculations treating a large number of local moments in a supercell [34] but attempting to use such an approach to construct a partition function is not feasible. Instead, a mean-field approximation (MFA) is made using a ‘‘reference’’ grand potential,

$$\Omega_0(\{\hat{\boldsymbol{e}}_i\}) = - \sum_i \boldsymbol{h}_i \cdot \hat{\boldsymbol{e}}_i, \quad (\text{A3})$$

where the vectors $\{\boldsymbol{h}_i\}$ correspond to the set of Weiss fields. The probability distribution can be written as a product of single-site probabilities $P_{0i}(\hat{\boldsymbol{e}}_i)$:

$$P_0(\{\hat{\boldsymbol{e}}_i\}) = \frac{1}{Z_0} \exp[-\beta \Omega_0(\{\hat{\boldsymbol{e}}_i\})] = \prod_i P_{0i}(\hat{\boldsymbol{e}}_i), \quad (\text{A4})$$

with $Z_0 = \prod_i Z_{0i}$, where

$$P_{0i}(\hat{\boldsymbol{e}}_i) = \frac{1}{Z_{0i}} \exp[\beta \boldsymbol{h}_i \cdot \hat{\boldsymbol{e}}_i]. \quad (\text{A5})$$

The partition function is also rewritten in terms of the Weiss field,

$$Z_{0i} = \int \exp[\beta \boldsymbol{h}_i \cdot \hat{\boldsymbol{e}}_i] d\hat{\boldsymbol{e}}_i = \frac{4\pi}{\beta h_i} \sinh(\beta h_i). \quad (\text{A6})$$

The free energy is, thus, given as

$$F(T) = \langle \Omega \rangle_{0,T} - TS, \quad (\text{A7})$$

$$= \langle \Omega \rangle_{0,T} + \frac{1}{\beta} \sum_{i=1}^N \int P_{0i}(\hat{\boldsymbol{e}}_i) \log P_{0i}(\hat{\boldsymbol{e}}_i) d\hat{\boldsymbol{e}}_i, \quad (\text{A8})$$

where $\langle \Omega \rangle_{0,T}$ is the DFT grand potential at temperature T calculated with respect to the model probability $P_0(\{\hat{\boldsymbol{e}}_i\})$ and S the magnetic entropy. The Weiss field at site i is given by

$$\boldsymbol{h}_i = -\nabla_{\boldsymbol{m}_i} \langle \Omega \rangle_{0,T}, \quad (\text{A9})$$

$$= -\frac{3}{4\pi} \int \hat{\boldsymbol{e}}_i \langle \Omega \rangle_{0,T}^{\hat{\boldsymbol{e}}_i} d\hat{\boldsymbol{e}}_i, \quad (\text{A10})$$

where $\langle \Omega \rangle_{0,T}^{\hat{\boldsymbol{e}}_i}$ denotes the thermal average and integrates over all the orientations except that at the site of interest, $\hat{\boldsymbol{e}}_i$ [42]. These averages are performed within the coherent potential

approximation. The local order parameters at different sublattices are defined as

$$\begin{aligned} \mathbf{m}_i(T) &\equiv \langle \hat{\mathbf{e}}_i \rangle_{0,T} \\ &= \int d\hat{\mathbf{e}}_i \frac{\hat{\mathbf{e}}_i \exp[\beta \mathbf{h}_i \cdot \hat{\mathbf{e}}_i]}{Z_{0i}} \prod_{j \neq i} \int d\hat{\mathbf{e}}_j \frac{\exp[\beta \mathbf{h}_j \cdot \hat{\mathbf{e}}_j]}{Z_{0j}} \\ &= \hat{\boldsymbol{\lambda}}_i L(\lambda_i), \end{aligned} \quad (\text{A11})$$

where dimensionless quantities $\lambda_i = \beta \mathbf{h}_i$ and unit vectors $\hat{\boldsymbol{\lambda}}_i = \lambda_i / |\lambda_i|$ ($\lambda_i = |\lambda_i|$) are introduced and $L(\lambda_i)$ is the Langevin function, $L(\lambda_i) = \coth(\lambda_i) - 1/\lambda_i$.

In numerical calculations, an adaptive algorithm [78] is employed for the BZ integration and a grid of 240×40 is used for the integration with respect to the angles of θ_i and ϕ_i of the magnetic local moment, respectively. The Weiss field obtained from Eq. (A10) is solved with an iterative scheme for every local-moment site in the unit cell [37,38]. Starting from uniform values at each site; i.e., the zeroth round, the values of the Weiss fields are updated by using results of the previous round, i.e.,

$$\lambda_j^{\text{next}} = \lambda_i^{\text{prev}} \frac{h_j^{\text{prev}}}{h_i^{\text{prev}}}, \quad (\text{A12})$$

where the Weiss field at site j in previous round, h_j^{prev} , is normalized by that at site i , h_i^{prev} . Then the temperature is evaluated from the relationship between input λ^{in} and output

h^{out} which is satisfied at self-consistency, $\beta h^{\text{out}} = \lambda^{\text{in}}$, thus,

$$T = \frac{1}{k_B} \frac{h^{\text{out}}}{\lambda^{\text{in}}}. \quad (\text{A13})$$

We consider self-consistency to have been achieved if the iterative temperature difference becomes less than the convergence criterion of 1 K. In all models, for temperatures within the range of 0–500 K self-consistency in the Weiss fields is achieved within five or six rounds.

An adjustment of the Fermi energy between the scalar-relativistic ferromagnetic calculation at zero temperature and the chemical potential for the fully relativistic DLM calculation at a finite temperature is needed so that the density of states integrates to the number of occupied electronic states. It is important that the chemical potential is accurately determined when estimating the spin polarization because of its sensitivity to the band filling near the Fermi energy. We achieve this aim by tuning the chemical potential

$$\mu_{\text{next}} = \mu_{\text{prev}} + \frac{N_{\text{val}}^{\text{desired}} - N_{\text{val}}^{\text{numeric}}}{D(E_F)} \quad (\text{A14})$$

within the above iterative procedure as done in Refs. [37] and [43]. Here μ_{next} (μ_{prev}) is the chemical potential for the next (previous) round, $N_{\text{val}}^{\text{desired}}$ is desired number of valence electrons, $N_{\text{val}}^{\text{numeric}}$ is numerically calculated number of valence electrons from the integrated DOS, and $D(E_F)$ is the total DOS at Fermi energy.

-
- [1] S. Bhatti, R. Sbiaa, A. Hirohata, H. Ohno, S. Fukami, and S. Piramanayagam, *Mater. Today* **20**, 530 (2017).
- [2] B. Dieny, R. B. Goldforb, and K. J. Lee, *Introduction to Magnetic Random-access Memory* (Wiley, New York, 2016).
- [3] K. Fujiwara, M. Oogane, A. Kanno, M. Imada, J. Jono, T. Terauchi, T. Okuno, Y. Aritomi, M. Morikawa, M. Tsuchida, N. Nakasato, and Y. Ando, *Appl. Phys. Exp.* **11**, 023001 (2018).
- [4] R. A. de Groot, F. M. Mueller, P. G. van Engen, and K. H. J. Buschow, *Phys. Rev. Lett.* **50**, 2024 (1983).
- [5] S. Ishida, S. Fujii, S. Kashiwagi, and S. Asano, *J. Phys. Soc. Jpn.* **64**, 2152 (1995).
- [6] I. Galanakis, P. H. Dederichs, and N. Papanikolaou, *Phys. Rev. B* **66**, 174429 (2002).
- [7] P. J. Webster, *J. Phys. Chem. Solids* **32**, 1221 (1971).
- [8] Y. Miura, K. Nagao, and M. Shirai, *Phys. Rev. B* **69**, 144413 (2004).
- [9] S. Picozzi, A. Continenza, and A. J. Freeman, *Phys. Rev. B* **69**, 094423 (2004).
- [10] K. Yakushiji, K. Saito, S. Mitani, K. Takanashi, Y. K. Takahashi, and K. Hono, *Appl. Phys. Lett.* **88**, 222504 (2006).
- [11] T. Mizuno, Y. Tsuchiya, T. Machita, S. Hara, D. Miyauchi, K. Shimazawa, T. Chou, K. Noguchi, and K. Tagami, *IEEE Trans. Magn.* **44**, 3584 (2008).
- [12] T. Iwase, Y. Sakuraba, S. Bosu, K. Saito, S. Mitani, and K. Takanashi, *Appl. Phys. Express* **2**, 063003 (2009).
- [13] Y. Sakuraba, K. Izumi, T. Iwase, S. Bosu, K. Saito, K. Takanashi, Y. Miura, K. Futatsukawa, K. Abe, and M. Shirai, *Phys. Rev. B* **82**, 094444 (2010).
- [14] Y. K. Takahashi, A. Srinivasan, B. Varaprasad, A. Rajanikanth, N. Hase, T. M. Nakatani, S. Kasai, T. Furubayashi, and K. Hono, *Appl. Phys. Lett.* **98**, 152501 (2011).
- [15] S. Li, Y. K. Takahashi, T. Furubayashi, and K. Hono, *Appl. Phys. Lett.* **103**, 042405 (2013).
- [16] J. W. Jung, Y. Sakuraba, T. T. Sasaki, Y. Miura, and K. Hono, *Appl. Phys. Lett.* **108**, 102408 (2016).
- [17] Y. Sakuraba, M. Hattori, M. Oogane, Y. Ando, H. Kato, A. Sakuma, T. Miyazaki, and H. Kubota, *Appl. Phys. Lett.* **88**, 192508 (2006).
- [18] N. Tezuka, N. Ikeda, A. Miyazaki, S. Sugimoto, M. Kikuchi, and K. Inomata, *Appl. Phys. Lett.* **89**, 112514 (2006).
- [19] S. Tsunegi, Y. Sakuraba, M. Oogane, K. Takanashi, and Y. Ando, *Appl. Phys. Lett.* **93**, 112506 (2008).
- [20] T. Ishikawa, N. Itabashi, T. Taira, K. i. Matsuda, T. Uemura, and M. Yamamoto, *Appl. Phys. Lett.* **94**, 092503 (2008).
- [21] N. Tezuka, N. Ikeda, F. Mitsuhashi, and S. Sugimoto, *Appl. Phys. Lett.* **94**, 162503 (2009).
- [22] H.-X. Liu, Y. Honda, T. Taira, K. I. Matsuda, M. Arita, T. Uemura, and M. Yamamoto, *Appl. Phys. Lett.* **101**, 132418 (2012).
- [23] K. Moges, Y. Honda, H. X. Liu, T. Uemura, M. Yamamoto, Y. Miura, and M. Shirai, *Phys. Rev. B* **93**, 134403 (2016).
- [24] H. Liu, T. Kawami, K. Moges, T. Uemura, M. Yamamoto, F. Shi, and P. M. Voyles, *J. Phys. D: Appl. Phys.* **48**, 164001 (2015).
- [25] L. Chioncel, Y. Sakuraba, E. Arrighoni, M. I. Katsnelson, M. Oogane, Y. Ando, T. Miyazaki, E. Burzo, and A. I. Lichtenstein, *Phys. Rev. Lett.* **100**, 086402 (2008).

- [26] K. Miyamoto, A. Kimura, Y. Miura, M. Shirai, M. Ye, Y. Cui, K. Shimada, H. Namatame, M. Taniguchi, Y. Takeda, Y. Saitoh, E. Ikenaga, S. Ueda, K. Kobayashi, and T. Kanomata, *Phys. Rev. B* **79**, 100405(R) (2009).
- [27] P. Mavropoulos, M. Lezaic, and S. Blügel, *Phys. Rev. B* **72**, 174428 (2005).
- [28] Y. Miura, H. Uchida, Y. Oba, K. Abe, and M. Shirai, *Phys. Rev. B* **78**, 064416 (2008).
- [29] A. Sakuma, Y. Toga, and H. Tsuchiura, *J. Appl. Phys.* **105**, 07C910 (2009).
- [30] Y. Miura, K. Abe, and M. Shirai, *Phys. Rev. B* **83**, 214411 (2011).
- [31] B. Hu, K. Moges, Y. Honda, H. X. Liu, T. Uemura, M. Yamamoto, J. I. Inoue, and M. Shirai, *Phys. Rev. B* **94**, 094428 (2016).
- [32] C. H. Shang, J. Nowak, R. Jansen, and J. S. Moodera, *Phys. Rev. B* **58**, R2917(R) (1998).
- [33] S. Zhang, P. M. Levy, A. C. Marley, and S. S. P. Parkin, *Phys. Rev. Lett.* **79**, 3744 (1997).
- [34] B. L. Gyorffy, A. J. Pindor, J. Staunton, G. Stocks, and H. Winter, *J. Phys. F: Met. Phys.* **15**, 1337 (1985).
- [35] J. B. Staunton, S. Ostanin, S. S. A. Razee, B. L. Gyorffy, L. Szunyogh, B. Ginatempo, and E. Bruno, *Phys. Rev. Lett.* **93**, 257204 (2004).
- [36] J. B. Staunton, L. Szunyogh, A. Buruzs, B. L. Gyorffy, S. Ostanin, and L. Udvardi, *Phys. Rev. B* **74**, 144411 (2006).
- [37] M. Matsumoto, R. Banerjee, and J. B. Staunton, *Phys. Rev. B* **90**, 054421 (2014).
- [38] C. E. Patrick, S. Kumar, G. Balakrishnan, R. S. Edwards, M. R. Lees, E. Mendive-Tapia, L. Petit, and J. B. Staunton, *Phys. Rev. Materials* **1**, 024411 (2017).
- [39] C. E. Patrick and J. B. Staunton, *Phys. Rev. Materials* **3**, 101401(R) (2019).
- [40] J. B. Staunton, R. Banerjee, M. dos Santos Dias, A. Deak, and L. Szunyogh, *Phys. Rev. B* **89**, 054427 (2014).
- [41] A. Deak, E. Simon, L. Balogh, L. Szunyogh, M. dos Santos Dias, and J. B. Staunton, *Phys. Rev. B* **89**, 224401 (2014).
- [42] C. E. Patrick and J. B. Staunton, *Phys. Rev. B* **97**, 224415 (2018).
- [43] G. A. Marchant, C. E. Patrick, and J. B. Staunton, *Phys. Rev. B* **99**, 054415 (2019).
- [44] M. Ležaić, P. Mavropoulos, J. Enkovaara, G. Bihlmayer, and S. Blügel, *Phys. Rev. Lett.* **97**, 026404 (2006).
- [45] J. D. Aldous, C. W. Burrows, A. M. Sánchez, R. Beanland, I. Maskery, M. K. Bradley, M. dos Santos Dias, J. B. Staunton, and G. R. Bel, *Phys. Rev. B* **85**, 060403(R) (2012).
- [46] H. C. Kandpal, G. H. Fecher, and C. Felser, *J. Phys. D: Appl. Phys.* **40**, 1507 (2006).
- [47] M. Yamamoto, T. Ishikawa, T. Taira, G. Li, K. Matsuda, and T. Uemura, *J. Phys.: Cond. Matter* **22**, 164212 (2010).
- [48] G.-f. Li, Y. Honda, H.-x. Liu, K.-i. Matsuda, M. Arita, T. Uemura, M. Yamamoto, Y. Miura, M. Shirai, T. Saito, F. Shi, and P. M. Voyles, *Phys. Rev. B* **89**, 014428 (2014).
- [49] J. Korrynga, *Physica* **13**, 392 (1947).
- [50] W. Kohn and N. Rostoker, *Phys. Rev.* **94**, 1111 (1954).
- [51] M. Däne, M. Lüders, A. Ernst, D. Ködderitzsch, W. M. Temmerman, Z. Szotek, and W. Hergert, *J. Phys.: Condens. Matter* **21**, 045604 (2009).
- [52] J. P. Perdew and Y. Wang, *Phys. Rev. B* **45**, 13244 (1992).
- [53] P. Soven, *Phys. Rev.* **156**, 809 (1967).
- [54] G. M. Stocks, W. M. Temmerman, and B. L. Gyorffy, *Phys. Rev. Lett.* **41**, 339 (1978).
- [55] H. Ebert, D. Ködderitzsch, and J. Minar, *Rep. Prog. Phys.* **74**, 096501 (2011).
- [56] K. Nawa and Y. Miura, *RSC Adv.* **9**, 30462 (2019).
- [57] A. Akriche, H. Bouafia, S. Hiadsi, B. Abidri, B. Sahli, M. Elchikh, M. A. Timaoui, and B. Djebour, *J. Magn. Magn. Mater.* **422**, 13 (2017).
- [58] M. Ležaić, P. Mavropoulos, G. Bihlmayer, and S. Blügel, *Phys. Rev. B* **88**, 134403 (2013).
- [59] K. H. J. Buschow, P. G. van Engen, and R. Jongebreur, *J. Magn. Magn. Mater.* **38**, 1 (1983).
- [60] E. Sasioglu, L. M. Sandratskii, P. Bruno, and I. Galanakis, *Phys. Rev. B* **72**, 184415 (2005).
- [61] J. Thoene, S. Chadov, G. Fecher, C. Felser, and J. Kubler, *J. Phys. D: Appl. Phys.* **42**, 084013 (2009).
- [62] J. Kubler, G. H. Fecher, and C. Felser, *Phys. Rev. B* **76**, 024414 (2007).
- [63] D. Comtesse, B. Geisler, P. Entel, P. Kratzer, and L. Szunyogh, *Phys. Rev. B* **89**, 094410 (2014).
- [64] M. A. Zagrebin, V. V. Sokolovskiy, and V. D. Buchelnikov, *J. Phys. D: Appl. Phys.* **49**, 355004 (2016).
- [65] H. Yang, O. Boule, V. Cros, A. Fert, and M. Chshiev, *Sci. Rep.* **8**, 16530 (2018).
- [66] J. B. Staunton, *Rep. Prog. Phys.* **57**, 1289 (1994).
- [67] J. Kübler, *J. Phys.: Condens. Matter* **18**, 9795 (2006).
- [68] A. I. Liechtenstein, M. I. Katsnelson, V. A. Antropov, and V. P. Gubanov, *J. Magn. Magn. Mater.* **67**, 65 (1987).
- [69] M. Methfessel and J. Kübler, *J. Phys. F: Met. Phys.* **12**, 141 (1982).
- [70] M. Jullière, *Phys. Lett. A* **54**, 225 (1975).
- [71] Y. Sakuraba, J. Nakata, M. Oogane, H. Kubota, Y. Aondo, A. Sakuma, and T. Miyazaki, *Jpn. J. Appl. Phys.* **44**, L1100 (2005).
- [72] A. Hütten, S. Kämmerer, J. Schmalhorst, A. Thomas, and G. Reiss, *Phys. Stat. Sol. (a)* **201**, 3271 (2004).
- [73] R. Modak, K. Uchida, and Y. Sakuraba (private communication).
- [74] B. Hülsen, M. Scheffler, and P. Kratzer, *Phys. Rev. B* **79**, 094407 (2009).
- [75] H. C. Herper, B. Krumme, D. Ebke, C. Antoniak, C. Weis, A. Warland, A. Hütten, H. Wende, and P. Entel, *J. Appl. Phys.* **109**, 07E128 (2011).
- [76] A. H. MacDonald, T. Jungwirth, and M. Kasner, *Phys. Rev. Lett.* **81**, 705 (1998).
- [77] T. Scheike, H. Sukegawa, T. Ohkubo, K. Hono, and S. Mitani, *J. Phys. D: Appl. Phys.* **53**, 045001 (2020).
- [78] E. Bruno and B. Ginatempo, *Phys. Rev. B* **55**, 12946 (1997).